Block copolymer microstructures in the intermediate-segregation regime

M. W. Matsen and F. S. Bates

Citation: The Journal of Chemical Physics **106**, 2436 (1997); doi: 10.1063/1.473153
View online: http://dx.doi.org/10.1063/1.473153
View Table of Contents: http://scitation.aip.org/content/aip/journal/jcp/106/6?ver=pdfcov
Published by the AIP Publishing

Block copolymer microstructures in the intermediate-segregation regime

M. W. Matsen[a] and F. S. Bates
Department of Chemical Engineering and Materials Science, University of Minnesota, Minneapolis, Minnesota 55455

(Received 26 August 1996; accepted 1 November 1996)

A detailed examination of the intermediate-segregation regime of diblock copolymer melts is presented using the incompressible Gaussian chain model and self-consistent field theory (SCFT). We find that the competition between interfacial tension and chain stretching used to describe behavior in the strong-segregation regime also explains behavior in this regime. Phase transitions from lamellae (L) to cylinders (C) to spheres (S) occur due to the spontaneous curvature produced as the asymmetry in the diblock composition increases. Complex phases, gyroid (G), perforated lamellar (PL), and double diamond (D), have curvatures between those of L and C, and therefore they compete for stability along the L/C boundary. Nevertheless, only G exhibits a region of stability. To explain why, we recognize that interfacial tension prefers the formation of constant mean curvature (CMC) surfaces to reduce interfacial area, and chain stretching favors domains of uniform thickness so as to avoid packing frustration. While the classical structures, L, C, and S, are successful at doing both simultaneously, the complex phases are not. Of the complex phases, G is the least frustrated and consequently is stable at intermediate degrees of segregation. However, G becomes unstable in the strong-segregation regime because the relative penalty for packing frustration increases with segregation. The PL and D structures are simply too frustrated, and therefore are never stable. © *1997 American Institute of Physics.* [S0021-9606(97)50806-3]

I. INTRODUCTION

AB diblocks have become the model block copolymer system for examining microphase separation in the melt state,[1–3] because of their inherent simplicity. This molecular architecture consists of just two chemically distinct blocks, A and B, with one end from each covalently bonded together. Two quantities characterize the AB diblock copolymer, its total number of segments N and the fraction f of those that belong to the A block. In a melt, these molecules are well described as incompressible Gaussian chains with each segment occupying a fixed volume $1/\rho_0$. The entropy loss that results when the ends of a ''course-grained'' segment are stretched to a distance l is proportional to $(l/a)^2$, where a is the statistical segment length. In this work, we assume the diblock is conformationally symmetric where A and B segment have equal statistical lengths; the generalization to unequal lengths is straightforward.[4] The interaction between A and B segments is represented by a standard Flory–Huggins form with a strength controlled by a single parameter, χ. A positive value of χ corresponds to an unfavorable interaction between the unlike segments.

The product χN dictates the degree to which the A and B blocks segregate. When $\chi N \lesssim 10$, entropy dominates the energetic penalty of mixing A and B segments, resulting in a disordered phase. As χN increases, the A and B blocks segregate inducing an order–disorder transition (ODT). Because these blocks are chemically joined, the A and B domains remain microscopic, and consequently ordered periodic structures result. Figure 1 depicts the various documented geometries. The classical microstructures are flat lamellae (L), hexagonally-packed cylinders (C), and spheres arranged on body-centered cubic lattice (S). Recently several complex structures have been observed. A perforated lamellar (PL) structure[5] occurs when the thin minority layers of the L phase each develop an hexagonal array of passages through which the majority layers are connected. Also reported[6,7] is a bicontinuous structure with $Ia3d$ space-group symmetry, denoted the gyroid (G) phase, where the minority component domain forms two interweaving three-fold coordinated lattices. Another cubic structure, the ordered bicontinuous double diamond (D) phase, with $Pn3m$ symmetry and two four-fold coordinated lattices has been reported in the past,[8] but is now thought to have been a misidentified G phase.[9]

An attractive feature of block copolymer melts is that they are well described by mean-field theory, except for a small region along the ODT. Even in this region, fluctuation effects become small when the molecular weight is large.[10] Figure 2 shows the mean-field phase diagram for conformationally symmetric diblocks calculated using self-consistent field theory (SCFT).[3] In addition to the conventional S phase, theory predicts a second spherical (S_{cp}) phase where the spheres arrange in a close-packed lattice rather than the usual bcc one.[11] This S_{cp} phase occurs in a very narrow region along the ODT for $\chi N \geqslant 17.67$. The only complex structure predicted by the theory is the G phase. It extends between the L and C phases from $\chi N = 11.14$ to about 60. The PL structure is nearly stable along the L/G boundary consistent with where it is observed experimentally.[2,5] On the other hand, the D structure is rather unstable in accord with recent experimental evidence that it is not present in diblock copolymer systems.[2,9]

[a]Present address: Polymer Science Centre, University of Reading, Whiteknights, Reading RG6 6AF, UK.

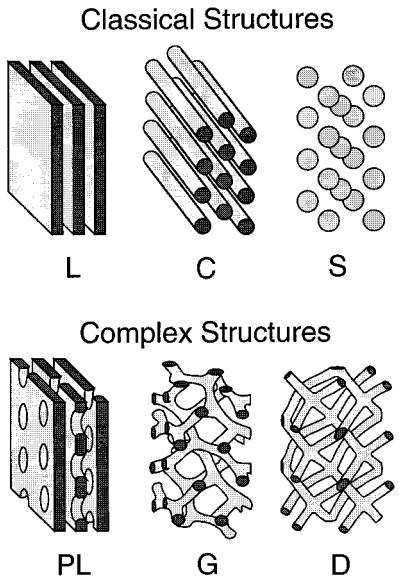

FIG. 1. Illustrations of six diblock copolymer microstructures showing the domains occupied by the minority component blocks. The majority component blocks fill the remaining space within the structures.

In the limit of large χN, diblock microstructures can be described by the strong-segregation theory (SST) of Semenov.[12] In fact, SCFT should reduce exactly to SST in the limit $\chi N \to \infty$ where the chains are strongly stretched.[13,14] However, exceptionally large values of χN are required for the strong-stretching assumption to become valid.[15] Nevertheless, SST is qualitatively correct, provides analytical expressions for the quantities of interest, and offers intuitive explanations for the phase behavior. In the SST, the free energy F of the melt takes the form

$$\frac{F}{nk_BT} = \mathscr{F}_{\rm el}^A + \mathscr{F}_{\rm el}^B + \mathscr{F}_{\rm int}, \tag{1}$$

$$= \alpha^A \left(\frac{R}{aN^{1/2}}\right)^2 + \alpha^B \left(\frac{R}{aN^{1/2}}\right)^2 + \beta(\chi N)^{1/2} \left(\frac{R}{aN^{1/2}}\right)^{-1}, \tag{2}$$

where n is the number of molecules in the melt, R is a measure of the domain size, and the coefficients, α^A, α^B, and β, are quantities that depend on the molecular composition f and the geometry of the microstructure. The first two terms, $\mathscr{F}_{\rm el}^A$ and $\mathscr{F}_{\rm el}^B$, account for entropic losses from stretching the A and B blocks, respectively. They are proportional to R^2 because the polymer chains are Gaussian. The last term, $\mathscr{F}_{\rm int}$, represents the interfacial energy and is proportional to the interfacial area which in turn is proportional to R^{-1}. Minimizing this free energy amounts to balancing entropic stretching energy against interfacial energy (i.e., $2\mathscr{F}_{\rm el}^A + 2\mathscr{F}_{\rm el}^B = \mathscr{F}_{\rm int}$). This determines the equilibrium domain size, which exhibits the well established scaling form,

$$R = a\left(\frac{\beta}{2(\alpha^A + \alpha^B)}\right)^{1/3} \chi^{1/6} N^{2/3}. \tag{3}$$

With that, the free energy expression, Eq. (2), reduces to

$$\frac{F}{nk_BT} = \frac{3}{2}\,(2(\alpha^A + \alpha^B)\beta^2 \chi N)^{1/3}. \tag{4}$$

In the appendix, we provide the coefficients, α^A, α^B, and β, for each of the classical phases. They are derived using a standard unit-cell approximation (UCA)[16] and ignoring exclusion zones.[17] Comparing the free energies, the lamellar (L) phase is stable for $0.299 < f < 0.701$, cylinders (C) are stable for $0.117 < f < 0.299$ or $0.701 < f < 0.883$, and spheres (S) occur for $f < 0.117$ or $0.883 < f$. Recent SST calculations for the complex phases, PL,[18] G,[19] and D,[20,21] predict them to be unstable in the strong-segregation limit consistent with Fig. 2.

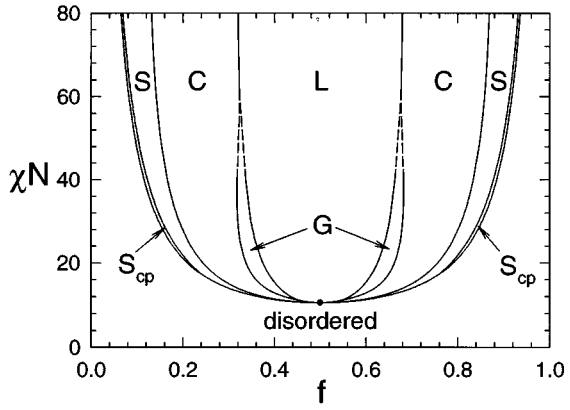

FIG. 2. Mean-field phase diagram for diblock copolymer melts calculated in Ref. 3. The ordered phases are labeled as L (lamellar), G (gyroid), C (cylindrical), S (spherical), and S_{cp} (close-packed spherical). The dot marks a mean-field critical point, and the dashed curves denote extrapolated phase boundaries, which could not be calculated due to numerical limitations.

This paper presents a study of the intermediate-segregation regime, $\chi N \sim 15$–60, using the SCFT of Helfand.[21] In this regime, neither the strong-segregation theory (SST) described above nor the weak-segregation theory of Leibler[22] provides an adequate description. For that reason, this intermediate regime has received less attention than the weak- and strong-segregation ones, even though it is experimentally more relevant. Although density functional theory[23] can be applied to this regime, the SCFT used here is superior because it avoids a number of approximations. The few SCFT calculations that have been performed[3,24,25] have focused primarily on phase boundaries. With the intention of explaining the phase behavior, we perform a more comprehensive study that examines numerous quantities such as segment distributions, individual contributions to the free energy, domain size, interfacial area, and interfacial curvature. We pay special attention to the latter, because it is possible to explain the intriguing complex phase behavior of diblock copolymer melts by studying the curvature of the surface that

divides the A- and B-rich domains.[26] At the strongest degree of segregation that we consider, $\chi N=60$, the A and B domains are nearly pure. Here, it becomes reasonable to compare SST to our SCFT results. Such a comparison reveals that while some quantities are well described by SST others are not. This is in part because the polymer chains are only weakly stretched contrary to the assumption in SST.[26] Nevertheless, we find that the SST is qualitatively correct at $\chi N=60$, and that, in fact, the SST description is conceptually valid over most of the intermediate-segregation regime.

II. SEGMENT DISTRIBUTIONS

A useful feature of a SCFT free energy calculation is that it yields the segment distributions. Here a selection of those distributions are examined, and these alone shed some light on the behavior of diblock melts in the intermediate-segregation regime. Specifically, we examine the overall A-segment distribution $\phi_A(\mathbf{r})$ and the distribution of the diblock junctions $\rho_J(\mathbf{r})$. (The dimensionless distribution $\phi_A(\mathbf{r})$ varies from 0 to 1 according to the fraction of segments at $\mathbf{r}$ that are of type A, and the junction distribution $\rho_J(\mathbf{r})$ is normalized so that its volume average is unity.) Figure 3 shows $\phi_A(\mathbf{r})$ (solid curves) and $\rho_J(\mathbf{r})$ (dashed curves) at a sequence of points across the phase diagram for $\chi N=20$. Because of the symmetry in the phase diagram, it is sufficient to examine the interval $f=1/2$–0, where A segments form the minority domain. We begin at $f=1/2$ showing the profile of the L phase, then we show profiles through the L and G phases at the L/G phase boundary, followed by G and C at the next boundary, C and S at the following boundary, and finally we show a profile of S_{cp} at the ODT. Figure 4 provides an analogous sequence for $\chi N=60$, except that profiles for the G phase are omitted because Fig. 2 indicates that it is unstable at this degree of segregation.

A number of observations can be made from Figs. 3 and 4. They demonstrate a substantial increase in segregation from $\chi N=20$–60. At the interface, this involves an increase in the slope of $\phi_A(\mathbf{r})$ and in the amplitude of $\rho_J(\mathbf{r})$. We note that at fixed χN, a slight decrease in segregation occurs as the ODT is approached. This is because A blocks become poorly anchored to the spherical microdomains as $f\rightarrow 0$, which results in a significant population of ''free chains.'' At large χN, this decrease in segregation tends to coincide with the S/S_{cp} transition for reasons that will be discussed in Sec. VII. Another observation is that the width of the minority domain decreases as the minority block becomes shorter, except when a phase transition occurs at which point it increases discontinuously. We will demonstrate in Sec. III that this is because a transition to a more curved microstructure allows the larger blocks to relax at the expense of the smaller blocks; i.e., the majority domain becomes thinner while the minority domain increases in thickness.

In the strong-segregation regime, the internal interface is narrow and relatively independent of the manner in which it is defined. At intermediate degrees of segregation, this is no longer the case, and therefore it is necessary to be careful when choosing a definition. When discussing interfacial energy, the interface is best defined as the locus, $\phi_A(\mathbf{r})=1/2$, where a maximum occurs in the internal energy density, which is proportional to $\chi\phi_A(\mathbf{r})\phi_B(\mathbf{r})$. Another natural definition is the locus of points where the distribution of diblock junctions $\rho_J(\mathbf{r})$ exhibits a peak. Mathematically, this condition can be expressed as $\nabla\phi_A(\mathbf{r})\cdot\nabla\rho_J(\mathbf{r})=0$. Both definitions produce similar results, but here the former is used because of its relevance to interfacial energy. Furthermore, the fact that this definition does not involve differentiation is numerically advantageous in our calculation because the Fourier representation of $\phi_A(\mathbf{r})$ converges more rapidly than, for example, that of $\nabla\phi_A(\mathbf{r})$.

In addition to the location of the interface, we are interested in the characteristic width over which the profile switches from A- to B-rich. Following a standard definition,[3] we define the interfacial width at a given point $\mathbf{r}$ on the interface as $w(\mathbf{r})=|\mathbf{n}_0\cdot\nabla\phi_A(\mathbf{r})|^{-1}$, where $\mathbf{n}_0$ is a unit vector normal to the interface. We find that this local interfacial width remains essentially constant over the entire surface of

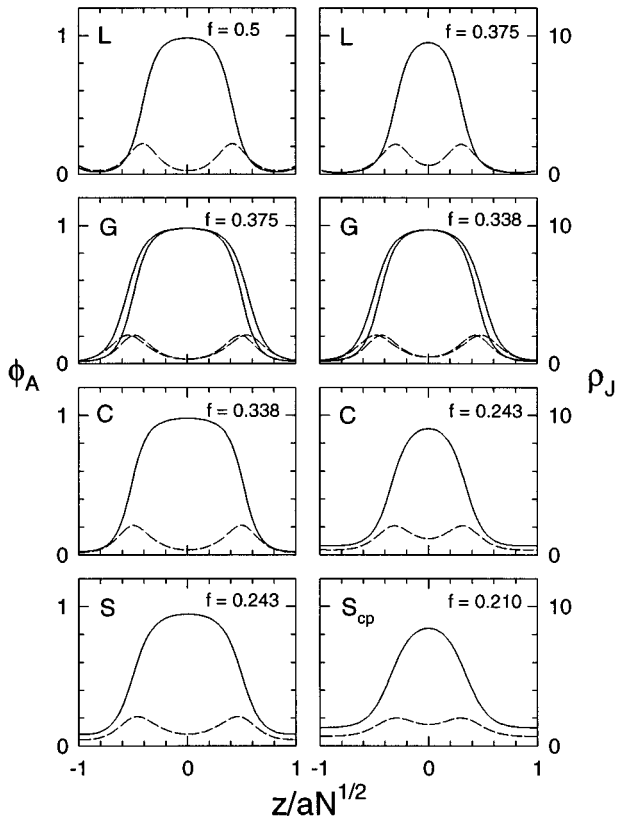

FIG. 3. A-segment profiles ϕ_A (solid curves) and diblock junction distributions ρ_J (dashed curves) are shown for a selection of compositions and phases at $\chi N=20$. In general, the coordinate z measures distance relative to the middle of a minority domain. The compositions $f=0.375$, 0.338, 0.243, and 0.210 correspond to the L/G, G/C, C/S, and S_{cp}/disordered phase boundaries. For the L and C structures, profiles are orthogonal to the layers and cylinders, respectively. For the C, S, and S_{cp} structures, profiles remain essentially invariant on this scale as the direction through minority domain is changed. For the G phase, profiles are provided for two orthogonal directions through the middle of a strut that forms its minority domain (see Fig. 1); these profiles differ because the cross-section of the strut is somewhat noncircular (see Fig. 14).

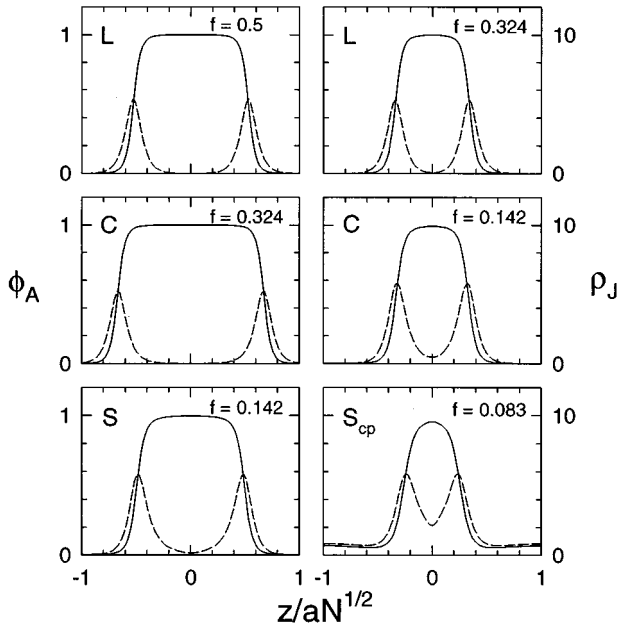

FIG. 4. Profiles and distributions analogous to those in Fig. 3, except that these are for $\chi N=60$. The G phase is excluded because it is thought to be unstable at this degree of segregation (see Fig. 2).

a microstructure. Therefore, it is meaningful to define a single area-averaged quantity,

$$w=\mathscr{A}^{-1}\int d\mathscr{A}|\mathbf{n}_0\cdot\nabla\phi_A(\mathbf{r})|^{-1}, \tag{5}$$

where $\mathscr{A}$ is the total interfacial area. Figure 5 shows the variation in this averaged interfacial width w across the phase diagram at constant χN. As the ODT is approached, there is a notable rise in the width consistent with the decrease in segregation observed above. At large degrees of segregation, w is relatively insensitive to f consistent with SST.[12]

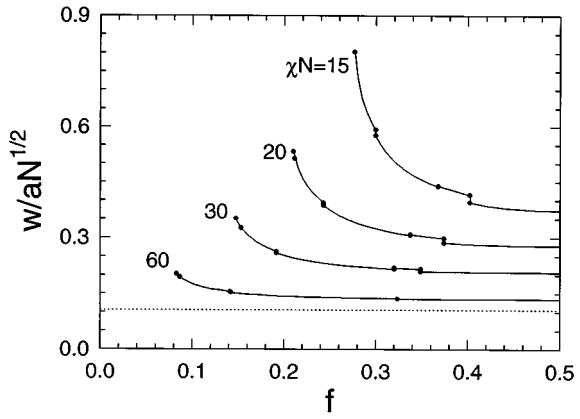

FIG. 5. Interfacial width w as a function of diblock composition f for several degrees of segregation χN. Dots indicate the phase transitions, many of which are evident from the discontinuities in w. Note that the G phase does not occur for $\chi N=60$. The dotted curve shows the SST prediction $w/aN^{1/2}=2/(6\chi N)^{1/2}$ with $\chi N=60$.

III. FREE ENERGY CONTRIBUTIONS

A natural strategy for understanding the phase behavior is to separate the free energy F into physically relevant contributions. This also provides the opportunity to examine in detail how well the diblock melts are represented by SST. Here we decompose the Helmholtz free energy as

$$F=U-T(S_J+S_A+S_B), \tag{6}$$

where U is the internal energy, S_J is the translational entropy of the junction, S_A is the configurational entropy of the A block, and S_B is the entropy of the B block. (Because we are examining an incompressible model, F and U could equally well be called the Gibbs potential and enthalpy, respectively.) Using the standard Gaussian model and SCFT, these quantities are given by

$$\frac{U}{nk_BT}=\frac{\chi N}{\mathscr{V}}\int d\mathbf{r}\phi_A(\mathbf{r})\phi_B(\mathbf{r}), \tag{7}$$

$$-\frac{S_J}{nk_B}=\frac{1}{\mathscr{V}}\int d\mathbf{r}\rho_J(\mathbf{r})\ln\rho_J(\mathbf{r}), \tag{8}$$

$$-\frac{S_A}{nk_B}=-\frac{1}{\mathscr{V}}\int d\mathbf{r}\{\rho_J(\mathbf{r})\ln q(\mathbf{r},f)+W_A(\mathbf{r})\phi_A(\mathbf{r})\}, \tag{9}$$

$$-\frac{S_B}{nk_B}=-\frac{1}{\mathscr{V}}\int d\mathbf{r}\{\rho_J(\mathbf{r})\ln q^{\dagger}(\mathbf{r},f)+W_B(\mathbf{r})\phi_B(\mathbf{r})\}, \tag{10}$$

where $\mathscr{V}\equiv nN/\rho_0$ is the total volume of the melt, and $q(\mathbf{r}',f)$ is the partition function of an A block subjected to the field $W_A(\mathbf{r})$ and constrained with its junction end fixed at $\mathbf{r}'$.[24] The analogous quantities for a B block are $q^{\dagger}(\mathbf{r}',f)$ and $W_B(\mathbf{r})$. The fields, $W_A(\mathbf{r})$ and $W_B(\mathbf{r})$, represent the molecular interactions experienced by A and B segments, respectively, at $\mathbf{r}$. They are determined by self-consistent relations,

$$W_A(\mathbf{r})=\chi N\phi_B(\mathbf{r})+\Xi(\mathbf{r}), \tag{11}$$

$$W_B(\mathbf{r})=\chi N\phi_A(\mathbf{r})+\Xi(\mathbf{r}), \tag{12}$$

where $\Xi(\mathbf{r})$ represents the hard-core interactions that enforce incompressibility, i.e., $\phi_A(\mathbf{r})+\phi_B(\mathbf{r})=1$.

In Figs. 6–9, the four contributions to the free energy are plotted as a function of f for four selected values of χN. In each plot, an inset shows the complex phase region at $\chi N=20$, comparing the two metastable states, PL and D, to the stable state, G. For the highest degree of segregation $\chi N=60$, the SST prediction is included for comparison. We note that in SST, the entropy of the junctions is ignored and the interfacial energy $\mathscr{F}_{\rm int}$ is half internal energy and half entropy, where the latter is split equally between the A and B blocks.[12] Therefore, the SST approximations are $U/nk_BT\approx\mathscr{F}_{\rm int}/2$, $-S_J/nk_B\approx 0$, $-S_A/nk_B\approx\mathscr{F}^A_{\rm el}+\mathscr{F}_{\rm int}/4$, and $-S_B/nk_B\approx\mathscr{F}^B_{\rm el}+\mathscr{F}_{\rm int}/4$.

The internal energy of the disordered state is $U/nk_BT=\chi Nf(1-f)$. Despite increasing χ, U initially decreases after crossing the ODT due to the development of order. This is reflected in Fig. 6 by the fact that the curve for $\chi N=20$ lies below the one for $\chi N=15$. By $\chi N\sim 25$, this

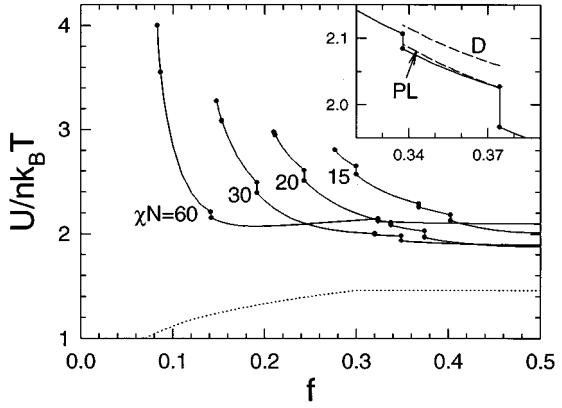

FIG. 6. Internal energy U as a function of diblock composition f for several degrees of segregation χN. Dots denote phase transitions. The dotted curve represents the SST prediction for $\chi N=60$. The inset shows the complex phase region at $\chi N=20$ with dashed curves denoting the metastable D and PL states.

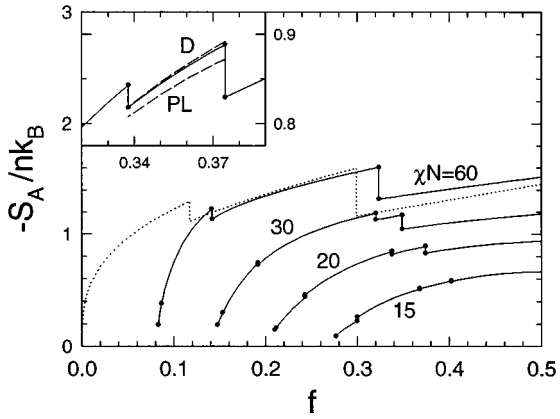

FIG. 8. Plot analogous to Fig. 6 showing the configurational entropy S_A of the A block.

trend begins to reverse and the internal energy increases. Eventually, it will increase proportionally to $(\chi N)^{1/3}$ as predicted by SST. We note that SST predicts no discontinuities in U at the order-order transitions consistent with our finding that the discontinuities calculated with SCFT become small as χN increases. Near the ODT, we see a sharp rise in the internal energy consistent with the decrease in segregation we observed previously. The inset in Fig. 6 shows that the D phase has a particularly high internal energy relative to the other complex phases; the reason for this will be provided in Sec. VI.

Figure 7 is straightforward to interpret. As the segregation increases and the diblock junctions become confined to the internal interface, the translational entropy decreases. This entropy is relatively constant with f except near the ODT where it increases, which is consistent with A blocks being pulled free from the minority domain providing more entropy for the junctions. As we will discuss later, the curves for $-S_J/nk_B$ will increase proportional to $\ln(\chi N)$ in the strong-segregation limit. Because this logarithmic dependence is eventually dominated by the power-law dependence of the other energy terms, the S_J contribution to the free energy is ignored in the SST.

The configurational entropies, S_A and S_B, of the A and B blocks show certain interesting behaviors. As f decreases from 1/2, the B blocks increase in size while the A blocks decrease; the entropies vary accordingly. However, at a transition, the discontinuous jumps in the entropies occur in the opposite directions. Specifically, $-S_A/nk_B$ in Fig. 8 increases at a transition to a more curved structure, with several exceptions at the weaker segregations. On the other hand, $-S_B/nk_B$ shown in Fig. 9 decreases at the transitions without exception. This is explained by the fact that, when a transition occurs to a structure with more interfacial curvature, the majority blocks relax while the minority ones stretch, consistent with the variation in the minority domain sizes observed in Sec. II. Taking note of the configurational entropies for the complex phases shown in the insets of Figs. 8 and 9 and keeping in mind that increasing interfacial curvature causes S_A to increase and S_B to decrease leads us to speculate that the sequence of phases, PL to G to D, repre-

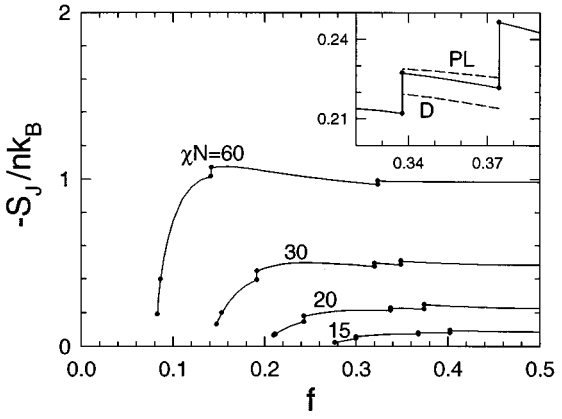

FIG. 7. Plot analogous to Fig. 6 showing the translational entropy S_J of the diblock junctions. Note that SST neglects this free energy contribution.

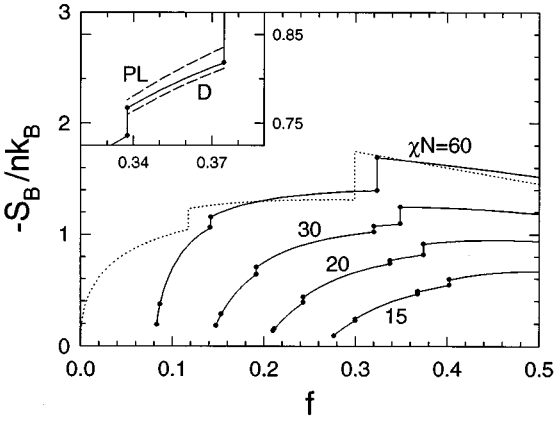

FIG. 9. Plot analogous to Fig. 6 showing the configurational entropy S_B of the B block.

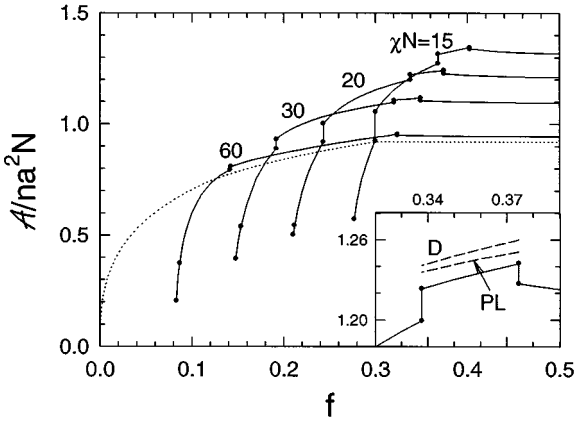

FIG. 10. Interfacial area $\mathscr{A}$ as a function of diblock composition f for a series of χN values. Dots denote phase transitions where $\mathscr{A}$ changes discontinuously. The dotted curve represents the SST prediction for $\chi N=60$. The inset shows the complex phase region at $\chi N=20$ with the metastable D and PL states represented by dashed lines.

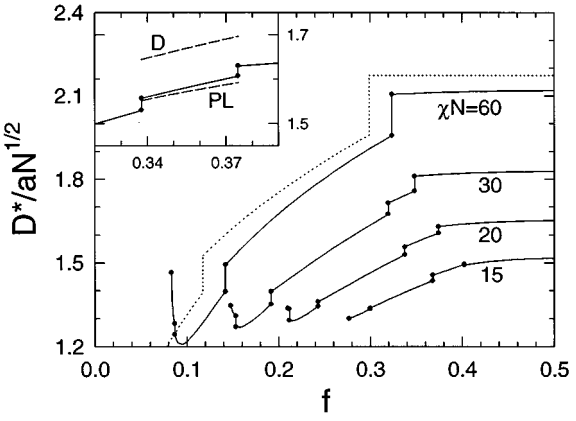

FIG. 11. Plot analogous to Fig. 10 showing the variation in the domain spacing $D^*=2\pi/q^*$, where q^* is the principle scattering vector. For the L and PL phases, the layer spacing equals D^*, for C the spacing between cylinders is $(4/3)^{1/2}D^*$, for S and S_{cp} the nearest-neighbor spacing of spheres is $(3/2)^{1/2}D^*$, for G the size of the cubic unit cell is $6^{1/2}D^*$, and for D the size of the unit cell is $2^{1/2}D^*$.

sents a monotonic increase in curvature. In Sec. V we will confirm that this is indeed the case.

IV. DOMAIN SIZE

The mechanisms controlling block copolymer phase behavior involve the interfacial tension between A- and B-rich domains and the entropic stretching energy of the polymers.[12] The interfacial tension acts to reduce the interfacial area $\mathscr{A}$ of the microstructure, and in doing so causes the domains spacing D^* to increase. This is countered by the entropic penalty of stretching the polymers so as to fill space at the middle of the domains.

Figure 10 shows a plot of the interfacial area $\mathscr{A}$ as a function of diblock composition f for a series of χN values. In general, an increase in χN produces a decrease in $\mathscr{A}$, but not always; for asymmetric compositions near the ODT, $\mathscr{A}$ increases with χN. Note that the complex phases (see the inset) all have substantially larger interfacial areas than the neighboring L and C phases for a reason that will become clear in Sec. VI. Figure 11 illustrates the variation in domain spacing D^* with changes in the diblock composition f for the same series of χN values. Here we define $D^*=2\pi/q^*$, where q^* is the principal scattering vector of a given structure. (For the S_{cp} structure, we define D^* using the face-centered cubic lattice.) Generally, the domain spacing shows a slow monotonic increase with segregation as expected. However, there is a sharp rise in the domain spacing of the spherical phases as the ODT is approached from any direction including decreasing χN. This is not anticipated by SST.

The curious behavior near the ODT, where $\mathscr{A}$ increases with χN and D^* becomes highly swollen, is consistent with our previous observations. When the minority blocks become short, many of them pull free from their domains swelling the matrix of the spherical phase. This causes the sharp rise in D^*. Furthermore, fewer diblock junctions are confined to the interface producing a significant reduction in $\mathscr{A}$. Examining the volume fractions of the minority and majority domains as the ODT is approached confirms that the nonlocalized diblocks are predominantly contained in the majority domain.

V. AVERAGE INTERFACIAL MEAN-CURVATURE

The sequence of phases, observed as the composition f of the diblock is varied, derives from the tendency for asymmetric diblocks to form curved interfaces. This is because placing an asymmetric diblock at a flat interface deforms the larger block more than the smaller one. In order to balance the relative deformations, the majority block requires more cross-sectional area than the minority block. The melt achieves this by curving the interface towards the minority blocks. In this Section, we demonstrate quantitatively the increase in interfacial curvature as the diblock composition varies from $f=1/2$ to either 0 or 1.

The curvature of a surface at a specified point is characterized by two principal curvatures, C_1 and C_2.[27] If the surface is defined as $\phi(\mathbf{r})=\phi_0$, the principal curvatures at a point $\mathbf{r}$ on the surface are calculated as follows. To start, three orthogonal unit vectors, one $\mathbf{n}_0\propto\nabla\phi(\mathbf{r})$ normal to the surface and two $\mathbf{n}_1$ and $\mathbf{n}_2$ parallel to the surface, are constructed. In the neighborhood of that point

$$\phi(\mathbf{r}+\xi\mathbf{n}_0+\eta\mathbf{n}_1+\zeta\mathbf{n}_2)\approx\phi_0+(\xi+\tfrac{1}{2}\eta^2G_{11}(\mathbf{r})+\eta\zeta G_{12}(\mathbf{r})+\tfrac{1}{2}\zeta^2G_{22}(\mathbf{r}))/w(\mathbf{r}),\tag{13}$$

where $G_{ij}(\mathbf{r})=w(\mathbf{r})\mathbf{n}_i\mathbf{n}_j:\nabla\nabla\phi(\mathbf{r})$ is the curvature tensor, $w(\mathbf{r})=|\mathbf{n}_0\cdot\nabla\phi(\mathbf{r})|^{-1}$ is the local interfacial width defined earlier, and ξ, η, and ζ are coordinates along the three orthogonal directions, $\mathbf{n}_0$, $\mathbf{n}_1$, and $\mathbf{n}_2$, respectively. The eigenvalues of the 2×2 matrix $G_{ij}(\mathbf{r})$ define the principal curvatures, while the eigenvectors provide the directions corresponding to these curvatures.

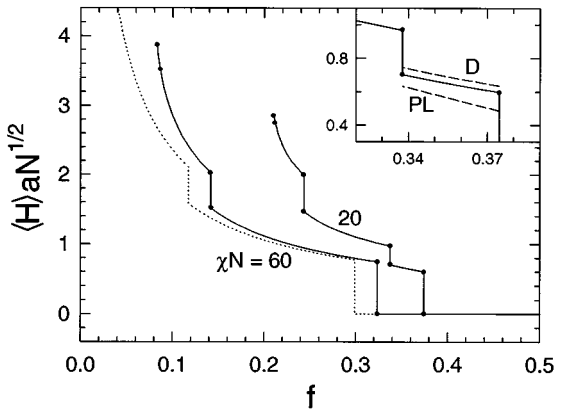

FIG. 12. Area-averaged mean curvature $\langle H\rangle$ as a function of diblock composition f for two degrees of segregation χN. The dots denote phase transitions, and the dotted curve represents the SST prediction for $\chi N=60$. The inset shows the complex phase region at $\chi N=20$ with the metastable D and PL metastable states represented by dashed curves.

From the principal curvatures, the mean curvature $H(\mathbf{r})$ at $\mathbf{r}$ is defined as

$$H(\mathbf{r}) \equiv \tfrac{1}{2}(C_1+C_2) = \tfrac{1}{2}\,\mathrm{Tr}\,G(\mathbf{r}) = \tfrac{1}{2}(G_{11}(\mathbf{r})+G_{22}(\mathbf{r})). \tag{14}$$

This quantity dictates how a surface element $d\mathscr{A}$ varies as it is translated normal to the interface. Specifically, the area element changes by a factor of $1\pm 2H(\mathbf{r})\xi+O(\xi^2)$, when translated from the surface by a distance ξ;[27] the area element increases on the convex side and decreases on the concave side of the interface. Thus, asymmetric diblocks prefer a finite $H(\mathbf{r})$ with the larger block on the convex side. As we will discuss later, $H(\mathbf{r})$ tends to remain uniform over the surface of the microstructure, and thus the area-averaged quantity,

$$\langle H\rangle = \mathscr{A}^{-1}\int d\mathscr{A} H(\mathbf{r}), \tag{15}$$

provides a good representative measure of the interfacial curvature for a given structure.

In Fig. 12, we plot the interfacial curvature as a function of f for two degrees of segregation. As expected, $\langle H\rangle$ increases monotonically as the molecule becomes asymmetric. Furthermore the curvature decreases with segregation, as it should since curvature scales inversely with domain size. The inset in Fig. 12 compares the complex G, PL, and G phases for the less segregated case, $\chi N=20$. The PL phase has a smaller curvature than the G phase, which explains why it is most preferred along the L/G transition. Likewise, the higher curvature of the D structure makes it least unstable along the C/G transition.

We have provided the reason for the occurrence of a complex phase region; complex structures offer intermediate curvatures to those of the C and L phases. However, we have not explained why the PL and D structures are omitted from the sequence of stable phases. Furthermore, up to this point, the discussion has offered no reason why the stability region of the G phase narrows with increasing χN, eventually becoming unstable at $\chi N\sim 60$. These points are taken up in the following section.

VI. INTERFACIAL TENSION VERSUS PACKING FRUSTRATION

Our explanation for the complex phase behavior is based on a delicate interplay between interfacial tension and the packing of the molecules under the constraint of constant segment density. Interfacial tension acts to minimize interfacial area under the condition that the volume fractions of the A and B domains remain fixed. As pointed out by Thomas *et al.*[28] this favors surfaces of constant mean curvature (CMC). At the same time, the system tries to minimize packing frustration.[29] To do that, a structure favors domains that are relatively uniform in thickness so as to distribute the entropic stretching energy equally among the molecules. We will examine the balance between these two tendencies through the influence on the curvature of the internal interface. To illustrate how, we first consider the simplest nontrivial structure, the C phase.

The radius of a cylindrical interface in the C phase can be expressed as $r(\theta)=r_0(1-\delta\cos(6\theta)+\delta'\cos(12\theta)+\cdots)$. Here we examine how δ is affected by the various free energy contributions. (Generally, δ' is a couple orders of magnitude smaller than δ, and therefore we will ignore the higher harmonics.) Interfacial tension favors $\delta=0$ so as to produce a CMC surface minimizing interfacial area, the minority component blocks also prefer $\delta=0$ for uniform stretching, but the majority component blocks require $\delta\sim 0.03$ in order to maintain a reasonably uniform domain [i.e., $L_1\approx L_2$ in Fig. 13(a)]. Figure 13(b) shows the actual variation in δ with segregation χN calculated from SCFT for several values of f. The small magnitude of δ illustrates that the packing frustration, which results from deforming a cylindrical unit into the hexagonal unit cell, is almost entirely restricted to the corona. As the thickness of the corona increases, the majority domain becomes more uniform reducing the packing frustration. Hence, as f becomes small, there is less deviation from a circular interface. With a circular shape, the minority component is free from packing frustration and the interfacial area is minimized. This raises the question whether the nearly circular shape is primarily due to the tendency to minimize packing frustration in the minority domain or to minimize interfacial area. Strong segregation theory (SST) offers a way of answering this.

In the appendix, the coefficients, α^A, α^B, and β, are evaluated for the free energy expression in Eq. (2) using the unit cell depicted in Fig. 13(a), where the interface is given by $r(\theta)=r_0(1-\delta\cos(6\theta))$. These coefficients are expanded in powers of δ, the variation from a perfectly circular interface. For both $\alpha^A=\alpha_0^A+\alpha_2^A\delta^2+O(\delta^3)$ and $\beta=\beta_0+\beta_2\delta^2+O(\delta^3)$, there are no linear terms and coefficients for δ^2 are positive. This reflects the fact that the elastic energy of the minority domain and the interfacial tension prefer the

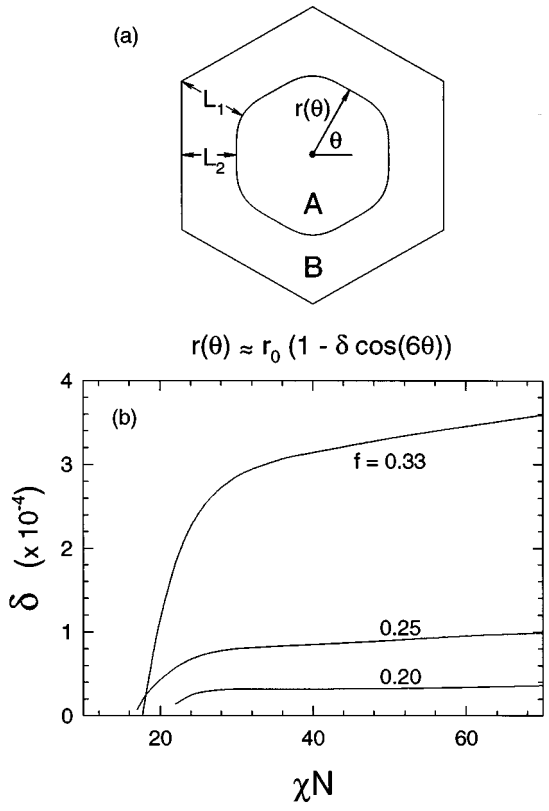

FIG. 13. (a) Wigner–Seitz unit cell for the C phase. The interfacial surface between A and B domains is approximated by $r(\theta)=r_0(1-\delta\cos(6\theta))$. In this figure, an exaggerated $\delta=0.03$ is used for demonstration purposes. (b) The actual variation in δ as a function of segregation χN calculated using SCFT for several diblock compositions f.

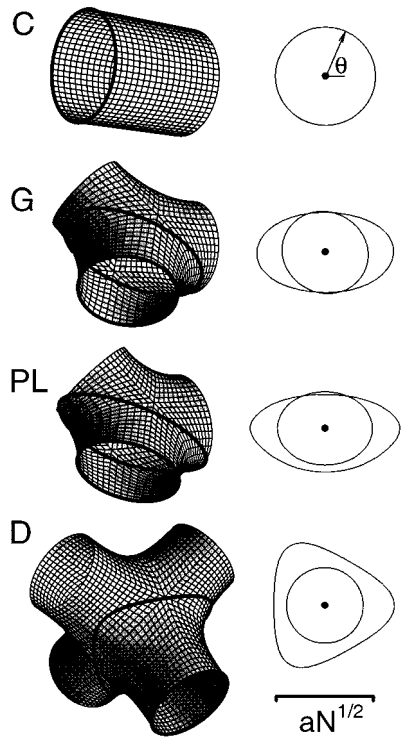

FIG. 14. On the left are three-dimensional plots of interfacial surfaces associated with elementary units of the C, G, PL, and D structures calculated at $\chi N=20$ and $f=0.338$ (the C/G phase boundary). Contours on the surfaces, indicated by bold curves, are shown in two-dimensional plots on the right.

circular interface, $\delta=0$. On the other hand, the linear term of α^B has a negative coefficient α_1^B, implying that packing frustration in the majority domain is relieved with a positive value of δ. Minimizing the free energy F with respect to R and expressing it as a power series in δ gives

$$F=F_0\left[1+\frac{\alpha_1^B}{\alpha_0^A+\alpha_0^B}\,\delta+\left(\frac{\alpha_2^A+\alpha_2^B}{\alpha_0^A+\alpha_0^B}+\frac{2\beta_2}{\beta_0}\right)\delta^2+O(\delta^3)\right], \tag{16}$$

where F_0 is the free energy of a circular ($\delta=0$) interface. The linear term in Eq. (16) results from the packing frustration in the majority domain, causing δ to deviate from zero. The quadratic term, which opposes this deviation, is dominated by the contribution due to the interfacial tension, $2\beta_2/\beta_0=35/2$. This implies that the tendency to form a CMC surface is the primary reason why δ remains small. In this SST calculation, $\delta=0.0030$, 0.0023, and 0.0019 for $f=0.33$, 0.25, and 0.20, respectively. Again, δ is smaller when the corona is thicker. However, δ is consistently much larger than it was for the finite segregations considered in Fig. 13(b), which indicates that the relative importance of packing frustration increases continuously with the degree of segregation.

As one may expect, the interfaces of the S and S_{cp} phases also show very little deviation from perfect spheres. In many cases, our numerical precision was not adequate to detect the incredibly small variations in the radius. Again as f is decreased and the corona becomes thicker the variations become smaller. We are reasonably certain that interfacial tension is again mostly responsible for minimizing deviations from CMC, but we have not done the analogous SST calculation to support this.

The cylindrical minority domains of the C phase are similar to the struts which are joined together into lattices to construct the complex phases (see Fig. 1). In Fig. 14, we compare elementary surface units from the C, G, PL, and D structures, evaluated at $\chi N=20$ along theC/G boundary using SCFT and the criterion $\phi_A(\mathbf{r})=1/2$. For each complex phase, we display the surface surrounding a junction of its lattice truncated by planes orthogonally cutting through the middle of each strut emerging from that junction. These plots illustrate that the lattices of the G and PL phases are three-fold coordinated, while those of the D phase are four-fold coordinated. On the surfaces in Fig. 14, we indicate selected contours using bold curves. For the C phase, a single contour orthogonal to the cylindrical axis is shown. For each complex phase, two contours orthogonal to the axis of a strut are indicated: One through the middle of the strut (the edge of our surface elements) and another near the junction. The contours are plotted two-dimensionally to the right and parameterized by an angle θ about the axis of the strut.

For each of the contours in Fig. 14, we plot the principal curvatures, C_1 and C_2, (dashed curves) and the mean curva-

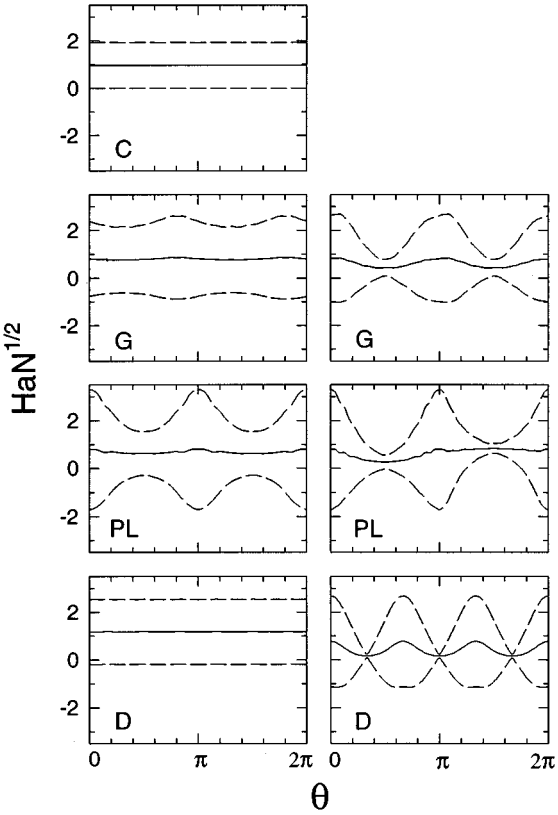

FIG. 15. Mean curvature, $H=(C_1+C_2)/2$, plotted along the contours shown in Fig. 14. The dashed curves denote the principal curvatures, C_1 and C_2. Plots on the left correspond to the contours along the edges of the elementary units in Fig. 14 (i.e., around the middle of a strut from the minority domain lattice), and plots on the right are from the contours near the centers of the elementary units.

ture, $H=(C_1+C_2)/2$, (solid curve) as a function of θ in Fig. 15. The C phase has one principal curvature that is identically zero and another that is nearly constant; this is characteristic of a circular cylinder. The curvatures along the contours located at the middle of the struts in the complex structures are shown in the plots on the left in Fig. 15. For the D phase, these curvatures are characteristic of circular tubelike struts. This is also somewhat true for the G phase, but not nearly so for the struts of the PL phase. The degree to which the struts become rodlike is related to their lengths. At $\chi N=20$ and $f=0.378$, the lengths l_s of the struts in the D, G, and PL structures are $l_s/aN^{1/2}=1.64$, 1.35, and 1.19, respectively. Keeping in mind that the different complex structures have majority domains of comparable thickness, the D phase has longer struts than G because its lattices are four- rather than three-fold coordinated and G has longer struts than PL because its lattices interpenetrate.

Although the principal curvatures vary significantly, the mean curvature is relatively uniform. Nevertheless, it is by no means constant as favored by the minimization of interfacial energy. To illustrate the variation in mean curvature, we plot its distribution, $d_{\mathscr{A}}(H)$, in Fig. 16 for the L, C, G, PL, and D structures at $\chi N=20$ and $f=0.378$. The quantity $d_{\mathscr{A}}(H)dH$ represents the amount of surface area with a mean curvature in the interval, H to $H+dH$. For the L

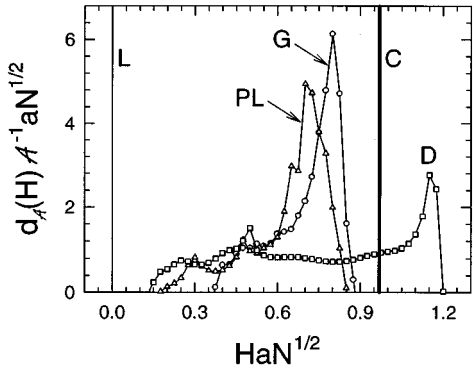

FIG. 16. Area distribution, $d_{\mathscr{A}}(H)$, of the mean curvature over the interfaces of the L, C, G, PL, and D structures at $\chi N=20$ and $f=0.338$ (the C/G phase boundary). The distribution for the L phase is proportional to a delta function, and the distribution for the C phase resembles a delta function on this scale.

phase, $d_{\mathscr{A}}(H)$ is proportional to a delta function located at $H=0$. For the C phase, it is nearly a delta function relative to the much broader distributions of the complex phases. To quantitatively express the broadness of these distributions, we evaluate the average $\langle H\rangle$ and standard deviation σ_H using

$$\langle H\rangle \equiv \mathscr{A}^{-1}\int dHHd_{\mathscr{A}}(H), \tag{17}$$

$$\sigma_H^2 \equiv \mathscr{A}^{-1}\int dH(H-\langle H\rangle)^2 d_{\mathscr{A}}(H). \tag{18}$$

These quantities are provided in Table I at various χN along the C/G phase boundary. The relative variation from CMC is best represented by the quantity, $\sigma_H/\langle H\rangle$, plotted in Fig. 17. This plot demonstrates that the complex phases are far from CMC in shape and furthermore that the deviation from CMC generally increases with segregation χN as concluded previously from Fig. 13(b).

Calculating $H(\mathbf{r})$ at a point $\mathbf{r}$ on the surface $\phi_A(\mathbf{r})=1/2$ requires particularly accurate evaluations of $\phi_A(\mathbf{r})$ because it must be differentiated twice [see Eq. (13)]. Although up to 450 independent Fourier terms were used to represent $\phi_A(\mathbf{r})$, we still experienced numerical inaccuracies when calculating $H(\mathbf{r})$. The PL phase is most affected, G is affected to a lesser degree, and D is relatively free of numerical inaccuracy. Presumably, the convergence for D is better than for PL and G because the density of independent wave vectors in Fourier space is smaller. In Fig. 15, some numerical noise

TABLE I. Variation in mean curvature, $\langle H\rangle aN^{1/2}\pm\sigma_H aN^{1/2}$, over the surfaces of the C, G, PL, and D structures at several points along the C/G phase boundary. The bracketed quantities may be somewhat inaccurate due to numerical inaccuracy.

χN	C	G	PL	D
30	0.885±0.006	0.644±(0.140)	0.572±(0.170)	0.682±0.315
25	0.923±0.005	0.671±0.130	0.602±0.150	0.711±0.315
20	0.970±0.003	0.704±0.121	0.636±0.146	0.747±0.311
15	1.035±0.010	0.743±0.105	0.668±0.158	0.793±0.287

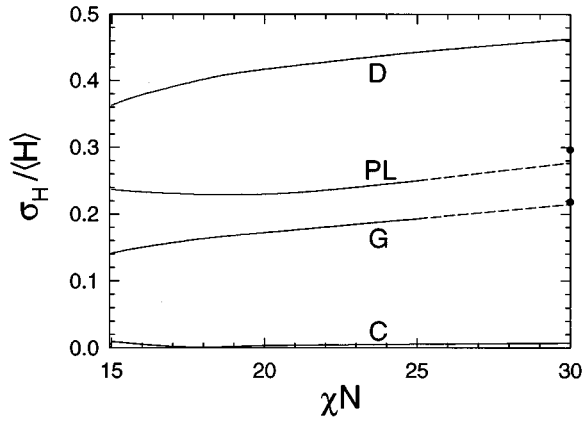

FIG. 17. Relative variation in mean curvature, $\sigma_H/\langle H\rangle$, over the surfaces of the C, G, PL, and D structures plotted as a function of χN along the C/G phase boundary. The dots denote our numerical values for the PL and G structures at $\chi N=30$, which are slightly inflated due to numerical inaccuracy in calculating σ_H. We expect that the extrapolations from $\chi N=25$ (dashed lines) are reasonably accurate.

is evident for the G and PL phases. This noise also affects $d_{\mathscr{A}}(H)$ to a degree that is noticeable in Fig. 16, but because the noise is oscillatory, it only weakly affects our evaluation of $\langle H\rangle$. However, it can cause σ_H to be significantly overestimated. At $\chi N=30$, we find this to be a problem for both the G and PL structures. The dots in Fig. 17 are our calculated values of $\sigma_H/\langle H\rangle$, while the dashed lines are extrapolated from the more accurate lower χN computations. Both results are relatively consistent, particularly the trends in $\sigma_H/\langle H\rangle$.

VII. DISCUSSION

Previous calculations on complex structures,[20,30] that were unable to optimize the shape of the interface, have assumed a constant mean curvature (CMC) surface. CMC surfaces have been generated for both bicontinuous cubic geometries examined here, G[31] and D.[27] At compositions corresponding to the complex phase region, these CMC surfaces have bulky junctions connected by narrow struts. As a consequence, a large disparity in the stretching energy results between blocks that fill the bulky junctions and those that occupy the narrow connecting struts. To relieve this frustration, the surface deviates from CMC so as to produce domains of more uniform thickness like those shown in Fig. 14. The reduction in packing frustration compensates the increased surface area that results from a non-CMC shape (see Fig. 10). The greater the frustration, the more the surface must deviate from CMC and the larger $\sigma_H/\langle H\rangle$ becomes. Thus, the size of this latter quantity reflects the inability of the structure to simultaneously minimize interfacial area and packing frustration, and therefore is related to the instability of the structure. Because the CMC surfaces for G have more uniform domains than those for D (see Refs. 27 and 31), G manages to maintain a more CMC-like interface and consequently is more stable than D.

It has been suggested[28] that as χ becomes large, the tendency to minimize surface area will ultimately dominate the tendency to form uniform domains, resulting in CMC-like structures. However, the competition between surface tension and entropic stretching maintains a balance between the two energies and prevents either tendency from completely dominating even in the strong-segregation limit. In fact, we have demonstrated that the tendency towards uniform domain thickness gradually increases over the tendency to minimize surface area. Consequently, the surfaces generally become less CMC-like as χ is increased contrary to earlier speculations [see Figs. 13(b) and 17]. Not surprisingly, packing frustration is greatest in the strong-segregation limit where chains are strongly stretched and therefore restricted to relatively few configurations.[13,15] Presumably, the regions in a domain that cause packing frustration are more easily filled when more configurations are accessible to the molecules. Following this line of reasoning, the G phase should become unstable at large χN because of its large packing frustration relative to that of the neighboring C and L phases. Note that the above arguments, claiming that packing frustration and therefore $\sigma_H/\langle H\rangle$ should increase with segregation, will not necessarily hold for small χN. So we are not too surprised by the decrease in $\sigma_H/\langle H\rangle$ that occurs for the PL structure up to $\chi N\sim 18$ in Fig. 17. What is relevant is that $\sigma_H/\langle H\rangle$ increases with χN at the higher degrees of segregation. Likewise, we are not concerned that δ becomes negative in Fig. 13(b) below $\chi N\sim 18$. The C phase is naturally close to CMC, and thus as the width of the interface becomes comparable to the domain size and its location becomes poorly defined, it is understandable that a negative value may occur contrary to our strong-segregation arguments.

Following ideas suggested by Gruner and co-workers,[6,29] the packing frustration in a block copolymer melt can be relieved by the addition of homopolymer. With the appropriate homopolymer, packing frustration can be relieved in either of the domains. Earlier SCFT calculations[32] have already shown that the addition of homopolymer to the minority domains of the G structure can cause a transition to the D phase. Alternatively, adding homopolymer to the majority domain can stabilize the PL phase. These results are easily explained. The four connectors of the D structure causes more packing frustration in the minority domain than the three connectors of either the G or PL structure. Once this is relieved by filling space at their centers with homopolymer, the D phase can become stable. The G and PL have similar minority domains, i.e., both are formed from three connectors, but the majority domains differ substantially. Evidently the majority domain of PL is more frustrated making it unstable. However, this can also be alleviated with homopolymer allowing PL to become stable. More recent calculations by Xi and Milner[33] suggest that homopolymer also stabilizes complex phases in the strong-segregation regime. In a forthcoming publication, we will provide a more complete examination of how the addition of homopolymer relieves packing frustration.

The occurrence of the S_{cp} phase along the ODT has been predicted earlier by Semenov.[11] This region occurs when the minority blocks become short allowing entropy to pull them from the spherical microdomains producing a substantial

population of unconstrained diblocks. These diblocks swell the matrix causing the rise in domain spacing observed in Fig. 11. The unconstrained diblocks relieve packing frustration in the majority domain, just as does the addition of homopolymer. As found in diblock/homopolymer blends,[32] this allows the spheres to switch from the body-centered cubic (bcc) packing. In this regime, the interaction between the spherical micelles is described by attractive two-body interactions,[11] which prefer a close-packed arrangement where the number of nearest neighbors is a maximum. Along the S/S_{cp} transition, we find that the hexagonally close-packed (hcp) arrangement is slightly favored over the face-centered cubic (fcc) one consistent with Ref. 11. Moving towards the ODT, Ref. 11 predicts the arrangement to alternate between hcp and fcc. Because of the difficulty in resolving the energy difference between them as the ODT is approached, we have not attempted to locate such transitions. In general, differences between the three arrangements of spheres, bcc, fcc, and hcp, are very small in the region near the ODT. In each case, the number of molecules per Wigner–Seitz unit cell is almost identical. Accordingly, the rearrangement of the spheres from bcc to close-packed is accompanied by an increase in the nearest-neighbor distance by a factor of about $2^{5/6}/3^{1/2}\approx 1.03$ in order to maintain the unit-cell volume (see Fig. 7). Other than that, the quantities calculated here are not affected significantly by the S/S_{cp} transition.

The PL phase also has a choice of packing arrangements that are nearly degenerate in free energy. Earlier[24] it was found that at weak segregations the perforated lamellae prefer to stack in the $abab\cdots$ sequence slightly more than in the $abcabc\cdots$ one. As the segregation increases, it becomes difficult to distinguish between the free energy of these two sequences. Pushing our calculation to higher precision, we now find that the $abcabc\cdots$ stacking becomes favored beyond $\chi N\sim 13$. The packing arrangement has a noticeable influence on the perforated layers. While the three-connectors are planar for the $abab\cdots$ sequence they are somewhat deformed in the $abcabc\cdots$ sequence. For $\chi N=20$ and $f=0.338$, the struts are tilted from planar by about 5°, which is the reason two contours for PL shown in Fig. 14 are shifted relative to each other.

The profiles in Fig. 4 illustrate that by $\chi N=60$, the diblock melt is well segregated except near the ODT where the S_{cp} phase occurs. At this degree of segregation, we might expect the SST to provide a good description of the melt. Indeed the domain spacings D^* predicted by SST agree well with the SCFT ones except near the ODT where the domain spacing swells and the S_{cp} phase becomes stable. The fact that D^* is predicted accurately by SST results in good agreement for the interfacial area $\mathscr{A}$ and average mean curvature $\langle H\rangle$ in Figs. 10 and 12, respectively. The agreement for the configurational entropy of the blocks, S_A and S_B, shown in Figs. 8 and 9, respectively, is also quite good. However, there are three quantities poorly represented by SST: The interfacial width w, the internal energy U, and the entropy of the junctions S_J. This can be attributed to the fact that SST ignores S_J. The justification for this is that the peak in $\rho_J(\mathbf{r})$ is proportional to $(w\mathscr{A})^{-1}$ which in the strong-segregation limit varies as $(\chi N)^{1/6}$. Thus S_J scales as $\ln(\chi N)$ where as U, S_A, and S_B all scale as $(\chi N)^{1/3}$; the latter follows from Eqs. (2) and (3). At sufficiently large χN, S_J becomes negligible relative to the other contributions to the free energy, but this does not happen until χN becomes extraordinarily large. For that reason, Semenov[34] has examined the effect of accounting for S_J, demonstrating that it results in a significantly wider interface. This brings the SST prediction of w into better agreement with SCFT.[3] Furthermore, the wider interface will increase U producing better agreement for that quantity as well.

VIII. CONCLUSIONS

We have performed a detailed study of diblock copolymers in the intermediate-segregation regime using the standard Gaussian chain model and self-consistent field theory (SCFT). This regime begins just slightly beyond the critical point, i.e., $\chi N\sim 15$, and extends to about $\chi N\sim 60$. Beyond that the melt is strongly segregated and is supposedly described by strong-segregation theory (SST). Although we find that at $\chi N=60$ some quantities are well described by SST, others are not. One source of inaccuracy is that SST ignores the translational entropy of the junctions S_J. This leads to inaccurate assessments of the internal energy U and the interfacial width w. Earlier work[15] has indicated a similar inaccuracy as a result of ignoring the entropy associated with the distribution of chain ends.

Although SST is not accurate at intermediate degrees of segregation, the explanations it provides for phase behavior are still valid in this regime. The principle mechanism involved is a competition between the interfacial energy and the entropic energy loss of stretching polymers so as to fill space. This competition sets the domain size. The geometry of the structure is chosen so as to best satisfy the spontaneous mean curvature of the internal interface. As the composition of the diblock evolves from symmetric ($f\sim 1/2$) to asymmetric ($f\sim 0$ or 1), the interfacial shape progresses from flat lamellae to highly curved spheres. The complex G phase is included in the sequence of stable phases because it offers an interfacial curvature intermediate to that of the L and C structures. However, this does not explain the absence of other complex phases, PL and D.

To complete the explanation for the complex phase behavior, we note that interfacial tension favors the formation of constant mean curvature (CMC) interfaces, while chain stretching favors domains of uniform thickness. The classical phases, L, C, and S, are successful in simultaneously satisfying both tendencies, but the complex phases, G, PL, and D, are not. For the complex phases, a CMC interface produces large variations in the domain thickness causing large degrees of packing frustration. To reduce this frustration, the interfaces are perturbed from CMC so as to produce more uniform domains. The residual packing frustration and the excess interfacial area resulting from a non-CMC shape disfavors the complex phases. While this prevents the stability of PL and D, the G phase remains stable at intermediate

xcdegrees of segregation. However, the relative penalty for packing frustration increases with χN, and consequently the G phase also becomes unstable in the strong-segregation regime, consistent with experiment.[35] These conclusions have motivated us to more carefully examine how the addition of homopolymer can be used to relieve packing frustration to increase the stability of the complex phases. The results of that study will be presented in a forthcoming paper.

ACKNOWLEDGMENTS

We thank D. A. Hajduk and M. A. Hillmyer for useful discussions and E. L. Thomas for providing us with a copy of Ref. 31. This work has been supported by the Minnesota Supercomputer Institute and by the National Science Foundation (DMR 94-05101).

APPENDIX

Here we provide the coefficients, α^A, α^B, and β, for the strong-segregation theory (SST) free energy expression, Eq. (2). We begin with the classical phases using the conventional unit-cell approximation (UCA)[16] and disregarding exclusion zones.[17] It has been demonstrated that the inaccuracy due to ignoring exclusion zones is absolutely negligible.[14] With the UCA, the L phase is treated exactly, but for the C and S phases the Wigner–Seitz cells are replaced by circular and spherical unit cells, respectively, of radius R. Given these approximations,[36]

$$\alpha^A=\begin{cases}\dfrac{\pi^2 f}{8}, & \text{for } L,\\ \dfrac{\pi^2}{16}, & \text{for } C,\\ \dfrac{3\pi^2}{80 f^{1/3}}, & \text{for } S,\end{cases} \tag{A1}$$

$$\alpha^B=\begin{cases}\dfrac{\pi^2(1-f)}{8}, & \text{for } L,\\ \dfrac{\pi^2(1-f^{1/2})^3(3+f^{1/2}),}{16(1-f)^2}, & \text{for } C,\\ \dfrac{3\pi^2(1-f^{1/3})^3(6+3f^{1/3}+f^{2/3})}{80(1-f)^2}, & \text{for } S,\end{cases} \tag{A2}$$

$$\beta=\begin{cases}\dfrac{1}{6^{1/2}}, & \text{for } L,\\ \dfrac{2 f^{1/2}}{6^{1/2}}, & \text{for } C,\\ \dfrac{3 f^{2/3}}{6^{1/2}}, & \text{for } S,\end{cases} \tag{A3}$$

where we assume A is the minority component (i.e., $f\leqslant 1/2$). By equating the volumes of the approximate and actual Wigner–Seitz cells, the principle domain spacings are calculated to be

$$D^*=\begin{cases}2R, & \text{for } L,\\ (3\pi^4/4)^{1/6}R, & \text{for } C,\\ (8\pi^2/9)^{1/6}R, & \text{for } S.\end{cases} \tag{A4}$$

Likhtman and Semenov[20] have provided a procedure for avoiding the UCA and considering arbitrarily shaped microdomains. Here, we apply it to the cylindrical (C) phase using the unit cell shown in Fig. 13(a), where the interface is given by $r(\theta)=r_0(1-\delta\cos(6\theta))$. In Ref. 20, it was assumed that the interface was a perfect circle (i.e., $r(\theta)=r_0$). With our more general interface,

$$\mathscr{F}_{\rm el}^A=\frac{9\pi^2}{2a^2Nf^2\mathscr{V}_{\rm cell}}\int_0^{\pi/6}d\theta\int_0^{r(\theta)}d\rho(\rho-r(\theta))^2\rho, \tag{A5}$$

$$\mathscr{F}_{\rm el}^B=\frac{9\pi^2}{2a^2N(1-f)^2\mathscr{V}_{\rm cell}}\int_0^{\pi/6}d\theta\int_{r(\theta)}^{R/\cos(\theta)}d\rho(\rho-r(\theta))^2\rho, \tag{A6}$$

$$\mathscr{F}_{\rm int}=\frac{2\sqrt{6}aN\chi^{1/2}}{\mathscr{V}_{\rm cell}}\int_0^{\pi/6}d\theta(r^2(\theta)+r'^2(\theta))^{1/2}, \tag{A7}$$

where the volume of the unit cell is $\mathscr{V}_{\rm cell}=2\sqrt{3}R^2$. Again we assume that A forms the cylindrical domains and B forms the matrix. The average radius r_0 of the cylinders is determined using

$$f\mathscr{V}_{\rm cell}=6\int_0^{\pi/6}d\theta r^2(\theta)=\pi r_0^2\left(1-\frac{1}{2}\delta^2\right). \tag{A8}$$

Expanding to second-order in δ, we obtain

$$\alpha^A=\frac{\sqrt{3}\pi}{8}(1+2\delta^2), \tag{A9}$$

$$\begin{aligned}\alpha^B=\frac{\sqrt{3}\pi}{8(1-f)^2}\Bigg(&\left[\frac{5\pi}{3\sqrt{3}}-(2\sqrt{3}\pi f)^{1/2}\left(\frac{4}{3}+\ln(3)\right)+6f-f^2\right]\\&-\left[(2\sqrt{3}\pi f)^{1/2}\left(\frac{116}{3}-35\ln(3)\right)+12\sqrt{3}\pi f+66f\right]\delta\\&+\left[(2\sqrt{3}\pi f)^{1/2}\left(\frac{1}{3}+\frac{1}{4}\ln(3)\right)-6\sqrt{3}\pi f\right.\\&\left.+\frac{327}{10}f-2f^2\right]\delta^2\Bigg),\end{aligned} \tag{A10}$$

$$\beta=\frac{1}{3}(\sqrt{3}\pi f)^{1/2}\left(1+\frac{35}{4}\delta^2\right). \tag{A11}$$

There are a number of approximations in the above calculation. Each block extends from the interface following a straight trajectory. In reality, they will follow curved paths and accounting for this will lower the free energy somewhat. In the Likhtman–Semenov formalism, the blocks extend outward normal to the interface. Here, we have them extending radially, but for small δ this difference becomes insignificant, and regardless they will not, in general, extend normal to the surface. This occurs in the Likhtman–Semenov formalism because they relax the constraint that the density of A and B blocks extending from the interface must be equal everywhere, due to the connectivity of the blocks. The alternative wedge-approach of Olmsted and Milner[36] does enforce this constraint. Despite the approximations used, the

above calculation is an accurate SST treatment of the C phase and should provide excellent estimates of δ in the strong-segregation limit.

[1] F. S. Bates and G. H. Fredrickson, Annu. Rev. Chem. **41**, 525 (1990).
[2] F. S. Bates, M. F. Schulz, A. K. Khandpur, S. Förster, J. H. Rosedale, K. Almdal, and K. Mortensen, Faraday Discuss. **98**, 7 (1994).
[3] M. W. Matsen and F. S. Bates, Macromolecules **29**, 1091 (1996).
[4] J. D. Vavasour and M. D. Whitmore, Macromolecules **26**, 7070 (1993); **29**, 5244 (1996); M. W. Matsen and M. Schick, *ibid*. **27**, 4014 (1994); M. W. Matsen and F. S. Bates, J. Polymer Sci. Part B (to be published).
[5] I. W. Hamley, K. Koppi, J. H. Rosedale, F. S. Bates, K. Almdal, and K. Mortensen, Macromolecules **26**, 5959 (1993).
[6] D. A. Hajduk, P. E. Harper, S. M. Gruner, C. C. Honeker, G. Kim, E. L. Thomas, and L. J. Fetters, Macromolecules **27**, 4063 (1994).
[7] M. F. Schulz, F. S. Bates, K. Almdal, and K. Mortensen, Phys. Rev. Lett. **73**, 86 (1994).
[8] E. L. Thomas, D. B. Alward, D. J. Kinning, D. C. Martin, D. L. Handlin, and L. J. Fetters, Macromolecules **19**, 2197 (1986).
[9] D. A. Hajduk, P. E. Harper, S. M. Gruner, C. C. Honeker, E. L. Thomas, and L. J. Fetters, Macromolecules **28**, 2570 (1995).
[10] G. H. Fredrickson and E. Helfand, J. Chem. Phys. **87**, 697 (1987).
[11] A. N. Semenov, Macromolecules **22**, 2849 (1989).
[12] A. N. Semenov, Sov. Phys. JETP **61**, 733 (1985).
[13] S. T. Milner, J. Polymer Sci. Part B **32**, 9698 (1994).
[14] M. W. Matsen and M. D. Whitmore, J. Chem. Phys. **105**, 000 (1996).
[15] M. W. Matsen and F. S. Bates, Macromolecules **28**, 8884 (1995).
[16] E. Helfand and Z. R. Wasserman, Macromolecules **11**, 960 (1978); **13**, 994 (1980).
[17] R. C. Ball, J. F. Marko, S. T. Milner, and T. A. Witten, Macromolecules **24**, 693 (1991); H. Li and T. A. Witten, *ibid*. **27**, 449 (1994).
[18] G. H. Fredrickson, Macromolecules **24**, 3456 (1991).
[19] P. D. Olmsted and S. T. Milner, Phys. Rev. Lett. **74**, 829 (1995).
[20] A. E. Likhtman and A. N. Semenov, Macromolecules **27**, 3103 (1994).
[21] E. Helfand, J. Chem. Phys. **62**, 999 (1975).
[22] L. Leibler, Macromolecules **13**, 1602 (1980).
[23] T. Ohta and K. Kawasaki, Macromolecules **19**, 2621 (1986); R. L. Lescanec and M. Muthukumar, *ibid*. **26**, 3908 (1993).
[24] M. W. Matsen and M. Schick, Phys. Rev. Lett. **72**, 2660 (1994).
[25] J. D. Vavasour and M. D. Whitmore, Macromolecules **25**, 5477 (1992); M. D. Whitmore and J. D. Vavasour, Acta Polymerica **46**, 341 (1995).
[26] M. W. Matsen and F. S. Bates, Macromolecules **29**, 7641 (1996).
[27] D. M. Anderson, H. T. Davis, L. E. Scriven, and J. C. C. Nitsche, Advances in Chem. Phys. **77**, 337 (1990).
[28] E. L. Thomas, D. M. Anderson, C. S. Henkee, and D. Hoffman, Nature **334**, 598 (1988).
[29] S. M. Gruner, J. Phys. Chem. **93**, 7562 (1989).
[30] D. M. Anderson and E. L. Thomas, Macromolecules **21**, 3221 (1988).
[31] K. Groβe-Brauckmann, The Family of Constant Mean-Curvature Gyroids, GANG Preprint, U-Mass, Amherst (1995).
[32] M. W. Matsen, Phys. Rev. Lett. **74**, 4225 (1995); Macromolecules **28**, 5765 (1995).
[33] H. Xi and S. T. Milner, Macromolecules **29**, 2404 (1996).
[34] A. N. Semenov, Macromolecules **26**, 6617 (1993); see Ref. 21 within.
[35] D. A. Hajduk, S. M. Gruner, P. Rangarajan, R. A. Register, L. J. Fetters, C. C. Honeker, R. J. Albalak, and E. L. Thomas, Macromolecules **27**, 490 (1994).
[36] P. D. Olmsted and S. T. Milner, Phys. Rev. Lett. **72**, 936 (1994).